Engineering Analysis with Boundary Elements 165 (2024) 105781

Contents lists available at ScienceDirect

Engineering Analysis with Boundary Elements

journal homepage: www.elsevier.com/locate/enganabound

Lattice Boltzmann method for variable viscous fluid flow on spherical surface

Junxiang Yang [a], Seungyoon Kang [b], Youngjin Hwang [b], Soobin Kwak [b], Seokjun Ham [b], Junseok Kim [b,*]

[a] School of Computer Science and Engineering, Faculty of Innovation Engineering, Macau University of Science and Technology, Macao Special Administrative Region of China

[b] Department of Mathematics, Korea University, Seoul 02841, Republic of Korea

ARTICLE INFO

Keywords:
Variable viscosity
Surface lattice Boltzmann method
Spherical surface

ABSTRACT

We propose an efficient numerical method for an incompressible fluid flow with variable viscosity on spherical surface. The proposed computational scheme is based on a finite volume lattice Boltzmann method (FVLBM). The spherical surface is triangulated and each point on the triangular mesh is assigned to one of two values of variable viscosity. Simplified coastlines using interpolation makes our proposed method highly efficient for solving fluid flows. Using the proposed algorithm, we simulate various fluid flows over inhomogeneous domains, i.e., land and sea areas. We apply different viscosity values for each domain using different relaxation times based on position of node points. Moreover, the progression of the storm is examined to demonstrate the effectiveness of the proposed approach.

1. Introduction

In recent years, tropical storms have occurred in many places on Earth, with some even developing into hurricanes, cyclones, and typhoons. These natural disasters cause a catastrophic amount of damage, particularly in coastal regions. Accordingly, there has been an urgent quest for fast and accurate storm event models. In this paper, we present a new method for analyzing storm behavior on the Earth's surface. Our method solves the incompressible surface Navier–Stokes (NS) equation on surface S using a finite volume lattice Boltzmann method (LBM).

LBM is a highly effective tool in computational fluid dynamics (CFD) technology. An earlier review of the application of LBM in fluid flow can be tracked back to [1]. Later, Aidum and Clausen [2] introduced developments of LBM on complex fluids before the year 2010. The LBM was developed based on an earlier idea of Lattice-Gas Cellular Automata; Wolf-Gladrow [3] reviewed these two methods in detail. Similarly, Succi [4] also reviewed the fluid models of LBM and introduced some potential applications. For the theories and engineering practices of LBM, interested readers can refer to [5,6]. Huang et al. [7] introduced practical LBM in multi-phase fluid simulations. As for a recent review of phase-field LBM in multi-phase fluid applications, please refer to [8] and references therein.

In recent years, some new progresses of LBM appears in fluid flow problems and aerodynamics. The phase-field based LBM [8–10] for multiphase flows were studied. The study of the mixed convention of nanofluids flow [11–13], garnered significant attention. Researchers also investigated laminar flow in both two-dimensional (2D) [13] and three-dimensional (3D) [14] domain. Furthermore, Mandzhieva and Subhankulova [15] applied the lattice Boltzmann model to study the pore-scale models. Babanezhad et al. [16] simulated the 3D cavity flow of a large dataset for the build-up fluid flow using LBM. Li et al. [17] introduced a LBM to describe interaction of waves and porous structures in 3D space. Hosseini et al. [18] reviewed various entropic LBMs and presented their recent progress and important challenges in that area.

The conventional LBM basically consists of two steps: moving the particle and relaxing distribution functions towards equilibrium. This coupling results restricts the LBM to Cartesian meshes [19–21]. Several extensions of LBM have been developed to overcome such restrictions. One of the pioneering work was done by He et al. [22], who added an interpolation step to the conventional LBM. Another noteworthy study is by Nannelli et al. [23], where Nannelli proposed a finite volume scheme for LBM. Since then, many works have been done using the finite volume scheme for LBM [24–26].

The above-mentioned studies only dealt with a fixed viscosity value. When substituting Earth into the problem, viscosity on land and sea has to be different. Therefore, we should solve LBM on a surface with various viscosity values. Here are some studies that considered surfaces

* Corresponding author.
E-mail address: cfdkim@korea.ac.kr (J. Kim).
URL: https://mathematicians.korea.ac.kr/cfdkim/ (J. Kim).

https://doi.org/10.1016/j.enganabound.2024.105781
Received 3 March 2024; Received in revised form 9 May 2024; Accepted 11 May 2024
Available online 20 May 2024

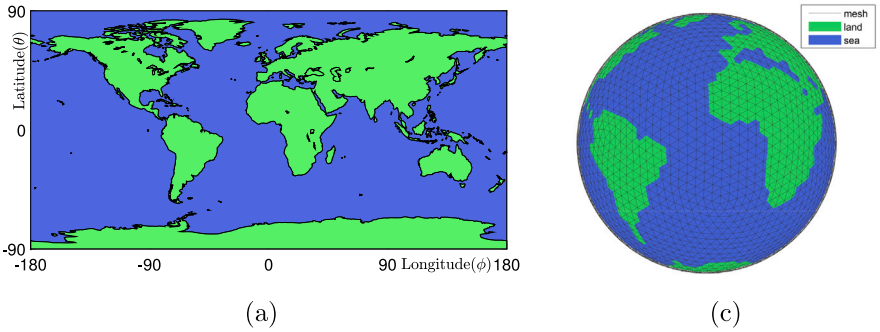

Fig. 1. (a) The world map in 2D space and (b) mapping on a spherical surface mesh. Here, green and blue colors denote land and sea regions, respectively.

with multiple viscosity values. Hussain et al. [27] demonstrated the flow behavior of a Casson fluid with variable viscosity that exhibits steady-state flow in 2D. The system is converted to an ODE, and numerical solutions are proposed. Chen et al. [28] presented an immersed boundary-simplified LBM for simulations of incompressible viscous flows. In this study, the relation between the relaxation parameter τ and viscosity ν is given as $\nu = c_s^2\left(\tau - \frac{1}{2}\right)\delta_t$. Guan and Novosselov [29] studied a numerical investigation of electroconvection phenomena between two parallel plates and proposed a two-relaxation time. The LBM is applied to fluids in porous media [30,31]. He et al. [30] studied the heat and mass transfer characteristics of a fluid with temperature-dependent viscosity using LBM. Li and Dimitrienko [31] studied the generalized Newtonian fluid in porous media using the homogenization method. After developing numerical methods, Li and Dimitrienko demonstrated the effects of viscosity on local problems. There are application of LBM to Navier–Stokes and convection–diffusion equations [32,33]. Chai and Baochang [32] presented a unified framework of multiple-relaxation-time LBM. Their model is depicted with a matrix that allows decoupled relaxation. Zhao et al. [33] proposed a block triple-relaxation-time LBM. One of the striking features of this model is that the model is partitioned into three relaxation parameter blocks. The relation between relaxation parameters is determined based on the analysis of the half-way bounce-back scheme.

In the previous work, we developed a finite volume scheme for the LBM on curved surfaces in 3D space [34], which used a constant viscosity. The main aim of this paper is to suggest an efficient numerical method for an incompressible fluid flow with variable viscosity on spherical surface so that we can simulate real-world scenarios where fluid viscosity changes with temperature or other fields.

The paper is organized as follows. In Section 2, we introduce the discretization of coastlines, which are simplified for calculation purpose. In Section 3, we present numerical results using LBM. Finally, in Section 4, we provide a brief conclusion.

2. Numerical method

2.1. Discretization of the computational domain

Fig. 1(a) and (b) illustrate the world map in 2D space and mapping on a spherical surface mesh, respectively. Green and blue colors denote land and sea regions, respectively. We use the 'load coastlines' command in the Mapping Toolbox to create a world map in MATLAB [35]. The 'load coastlines' command returns the coastline data in latitude ('coastlat') and longitude ('coastlon'). See Fig. 2(a) for the plot of coastlines, where the horizontal and vertical axes represent longitude ϕ and latitude θ, respectively.

For simplicity, we exclude small islands by removing coastlines with fewer than 100 points and coastlines that lie within another coastline. As shown in Fig. 2(b), this process results in only nine large coastlines. We further simplify the coastlines using an interpolation method and reduce the number of points for each coastline by a factor of five. Smooth interpolated coastlines are shown in Fig. 2(c). The spherical surface is discretized using a triangular mesh, as illustrated in Fig. 2(d). At each vertex point (x, y, z) of the triangular mesh, we find the corresponding angles $(\theta, \phi) = (\arcsin(z/R), \arctan(y/x))$, where θ, ϕ, and R are schematically illustrated in Fig. 2(e). Next, we find whether (θ, ϕ) is in a land or sea area. We define an indicator function $\mathbb{1}_c$ such that if (x, y, z) is in land, $\mathbb{1}_c(x, y, z) = 1$ and $\mathbb{1}_c(x, y, z) = 0$ when (x, y, z) is in the sea. Figs. 2(f) and (g) illustrate (x, y, z) points in green when $\mathbb{1}_c(x, y, z) = 1$ and in blue when $\mathbb{1}_c(x, y, z) = 0$, on 2D space and the spherical surface, respectively.

2.2. Finite volume lattice Boltzmann method

In this paper, we simulate variable viscous and incompressible fluid flow on a spherical surface by modifying the finite volume lattice Boltzmann equation proposed by Yang et al. [34]. Among the various methods for solving the lattice Boltzmann equation, we choose the finite volume method due to its applicability to arbitrarily shaped domains and irregular meshes [36]. In particular, we apply this method to a curved spherical surface. A disadvantage is its increased complex compared to the conventional LBM.

The governing equation of finite volume lattice Boltzmann method (FVLBM) is given as follows [37]:

$$\frac{\partial f_i}{\partial t}(\mathbf{x}, t) + \mathbf{c}_i \cdot \nabla f_i(\mathbf{x}, t) = -\frac{1}{\tau(\mathbf{x})}\left(f_i(\mathbf{x}, t) - f_i^{eq}(\mathbf{x}, t)\right), \ i = 1, 2, \ldots, 19. \quad (1)$$

For $\mathbf{x} = (x, y, z)$ and time t, $f_i(\mathbf{x}, t)$ and $f_i^{eq}(\mathbf{x}, t)$ are particle distribution function and local equilibrium distribution, respectively. ith directional velocity is $\mathbf{c}_i$. For $f_i(\mathbf{x}, t)$ and $\mathbf{c}_i$, index i varies from 1 to 19. $\tau(\mathbf{x})$ is the relaxation time at space $\mathbf{x}$. Values of $\mathbf{c}_i$ are given as follows:

$$\mathbf{c}_1 = (1, 0, 0), \mathbf{c}_2 = (-1, 0, 0), \mathbf{c}_3 = (0, 1, 0), \mathbf{c}_4 = (0, -1, 0),$$
$$\mathbf{c}_5 = (0, 0, 1), \mathbf{c}_6 = (0, 0, -1), \mathbf{c}_7 = (1, 1, 0), \mathbf{c}_8 = (1, -1, 0),$$
$$\mathbf{c}_9 = (1, 0, 1), \mathbf{c}_{10} = (1, 0, -1), \mathbf{c}_{11} = (-1, 1, 0), \mathbf{c}_{12} = (-1, -1, 0),$$
$$\mathbf{c}_{13} = (-1, 0, 1), \mathbf{c}_{14} = (-1, 0, -1), \mathbf{c}_{15} = (0, 1, 1), \mathbf{c}_{16} = (0, 1, -1),$$
$$\mathbf{c}_{17} = (0, -1, 1), \mathbf{c}_{18} = (0, -1, -1), \mathbf{c}_{19} = (0, 0, 0).$$

Eq. (1) is solved on surface S by discretizing the surface into a triangular mesh, shown in Fig. 3(a). Consider a point $\mathbf{P}$ on the mesh and points $\mathbf{P}_i$, $i = 1, 2, \ldots$, which are one-ring neighboring points of $\mathbf{P}$. In case of Fig. 3(a), i ranges from 1 to 6. Let $\mathbf{M}$ be the center of edge PP_1 and $\mathbf{G}$ be the centroid of triangle $\triangle PP_1P_2$. Integrating Eq. (1) over triangle $\triangle PMG$, we obtain the following equation:

$$\begin{aligned}\int_{\triangle PMG} \frac{\partial f_i}{\partial t}(\mathbf{x}, t)d\sigma + \int_{\triangle PMG} \mathbf{c}_i \cdot \nabla f_i(\mathbf{x}, t)d\sigma \\ = -\int_{\triangle PMG} \frac{1}{\tau(\mathbf{x})}\left(f_i(\mathbf{x}, t) - f_i^{eq}(\mathbf{x}, t)\right)d\sigma.\end{aligned} \quad (2)$$

We approximate and calculate each term of Eq. (2). The first term of left hand side can be approximated using $\frac{\partial f_i}{\partial t}(\mathbf{x}, t) \approx \frac{\partial f_i}{\partial t}(\mathbf{P}, t)$ for $\mathbf{x} \in \triangle PMG$. $A_{\triangle PMG}$ is the area of triangle $\triangle PMG$ at time t.

$$\int_{\triangle PMG} \frac{\partial f_i}{\partial t}(\mathbf{x}, t)d\sigma \approx \int_{\triangle PMG} \frac{\partial f_i}{\partial t}(\mathbf{P}, t)d\sigma = \frac{\partial f_i}{\partial t}(\mathbf{P}, t)\int_{\triangle PMG} d\sigma \quad (3)$$

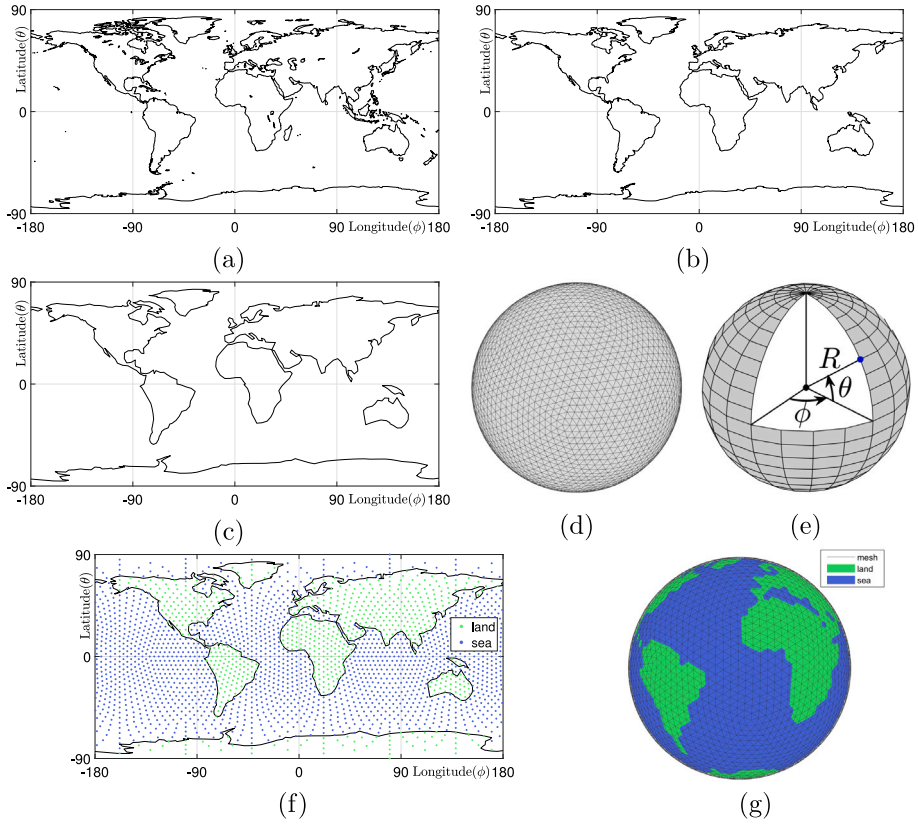

Fig. 2. (a) World Map using Mapping Toolbox. (b) Excluding small islands. (c) Applying an interpolation method for simplicity. (d) Discretizing the spherical surface using a triangular mesh. (e) Schematic illustration of θ and ϕ. (f) Illustration of (x, y, z) points in 2D space. (g) Illustration of (x, y, z) points on a spherical surface.

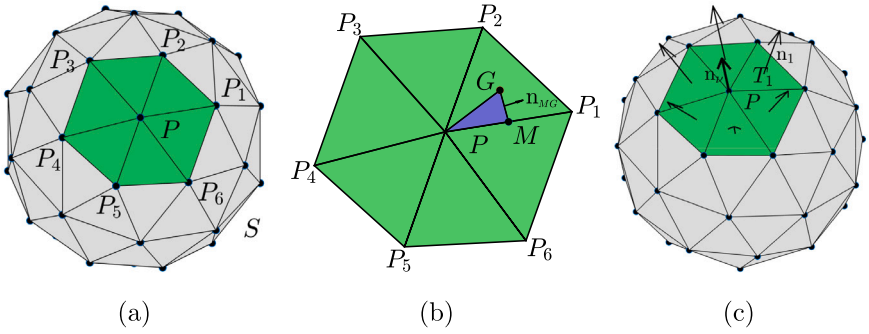

Fig. 3. Schematic diagram of (a) Triangular mesh. (b) Integration over triangle $\triangle PMG$. (c) velocity field correction.

$$= \frac{\partial f_i}{\partial t}(\mathbf{P}, t) A_{\triangle PMG} = \frac{f_i(\mathbf{P}, t + \Delta t) - f_i(\mathbf{P}, t)}{\Delta t} A_{\triangle PMG}.$$

The second term of left hand side of Eq. (2) is the flux, which can be calculated using the divergence theorem. $\mathbf{n}_{PM}$, $\mathbf{n}_{MG}$ and $\mathbf{n}_{GP}$ are outward normal vectors of edge PM, MG, and GP, respectively. See Fig. 3(b) for schematic diagram of $\mathbf{n}$. l_{PM}, l_{MG}, and l_{GP} are length of PM, MG, and GP, respectively.

$$\begin{aligned}
&\int_{\triangle PMG} \mathbf{c}_i \cdot \nabla f_i(\mathbf{x}, t) d\sigma = \int_{\triangle PMG} \nabla \cdot [f_i(\mathbf{x}, t)\mathbf{c}_i] d\sigma = \int_{\partial \triangle PMG} f_i(\mathbf{x}, t)\mathbf{c}_i \cdot \mathbf{n} dl \\
&= \int_{PM} f_i(\mathbf{x}, t)\mathbf{c}_i \cdot \mathbf{n}_{PM} dl + \int_{MG} f_i(\mathbf{x}, t)\mathbf{c}_i \cdot \mathbf{n}_{MG} dl + \int_{GP} f_i(\mathbf{x}, t)\mathbf{c}_i \cdot \mathbf{n}_{GP} dl \\
&= \frac{f_i(\mathbf{P}, t) + f_i(\mathbf{M}, t)}{2} \mathbf{c}_i \cdot \mathbf{n}_{PM} l_{PM} + \frac{f_i(\mathbf{M}, t) + f_i(\mathbf{G}, t)}{2} \mathbf{c}_i \cdot \mathbf{n}_{MG} l_{MG} \qquad (4) \\
&+ \frac{f_i(\mathbf{G}, t) + f_i(\mathbf{P}, t)}{2} \mathbf{c}_i \cdot \mathbf{n}_{GP} l_{GP}.
\end{aligned}$$

$\mathbf{n}_{MG}$ can be calculated using edges of triangle $\triangle PMG$. Other outward normal vectors can be calculated in the same way.

$$\mathbf{n}_{MG} = \frac{\overrightarrow{PG} - \overrightarrow{PG} \cdot \overrightarrow{MG} \frac{\overrightarrow{MG}}{|\overrightarrow{MG}|}}{\left| \overrightarrow{PG} - \overrightarrow{PG} \cdot \overrightarrow{MG} \frac{\overrightarrow{MG}}{|\overrightarrow{MG}|} \right|}.$$

Due to the fact that M is the center of PP_1 and G is centroid of triangle $\triangle PMG$, values of $f_i(\mathbf{M}, t)$ and $f_i(\mathbf{G}, t)$ can be calculated using interpolation.

$$f_i(\mathbf{M}, t) = \frac{f_i(\mathbf{P}, t) + f_i(\mathbf{P}_1, t)}{2}, \qquad (5)$$

$$f_i(\mathbf{G}, t) = \frac{f_i(\mathbf{P}, t) + f_i(\mathbf{P}_1, t) + f_i(\mathbf{P}_2, t)}{3}. \qquad (6)$$

On right hand side of Eq. (2), collision is approximated using interpolation similar to Eq. (6).

$$-\int_{\triangle PMG}\frac{1}{\tau(\mathbf{x})}\left(f_i(\mathbf{x},t)-f_i^{eq}(\mathbf{x},t)\right)d\sigma = -\frac{A_{\triangle PMG}}{\tau(\mathbf{P})}\left(\frac{f_i(\mathbf{P},t)+f_i(\mathbf{M},t)+f_i(\mathbf{G},t)}{3}-\frac{f_i^{eq}(\mathbf{P},t)+f_i^{eq}(\mathbf{M},t)+f_i^{eq}(\mathbf{G},t)}{3}\right). \tag{7}$$

Here, the local equilibrium f_i^{eq} is defined in the following way.

$$f_i^{eq}(\mathbf{x},t)=w_i\rho(\mathbf{x},t)\left[1+\frac{\mathbf{c}_i\cdot\mathbf{u}(\mathbf{x},t)}{c_s^2}+\frac{1}{2}\left(\frac{\mathbf{c}_i\cdot\mathbf{u}(\mathbf{x},t)}{c_s^2}\right)^2-\frac{|\,\mathbf{u}(\mathbf{x},t)\,|^2}{2c_s^2}\right], \tag{8}$$

where w_i is the lattice weight as following:

$$w_i=\begin{cases}\frac{2}{36}, & i=1,\dots,6,\\ \frac{1}{36}, & i=7,\dots,18,\\ \frac{12}{36}, & i=19,.\end{cases}$$

In this paper, the value of lattice speed of sound is $c_s=1/\sqrt{3}$ for the triangular mesh. Density $\rho(\mathbf{x},t)$ and velocity $\mathbf{u}(\mathbf{x},t)$ are calculated in the following way using $f_i(\mathbf{x},t)$ and $\mathbf{c}_i$.

$$\rho(\mathbf{x},t)=\sum_{i=1}^{19}f_i(\mathbf{x},t), \tag{9}$$

$$\mathbf{u}(\mathbf{x},t)=\frac{1}{\rho(\mathbf{x},t)}\sum_{i=1}^{19}f_i(\mathbf{x},t)\mathbf{c}_i. \tag{10}$$

Substituting Eqs. (3), (4) and (7) to Eq. (2), we get

$$f_i(\mathbf{P},t+\Delta t)=f_i(\mathbf{P},t)+\frac{\Delta t}{A_{\mathbf{P}}}\left(\text{Collision}_{\mathbf{P}}-\text{Flux}_{\mathbf{P}}\right) \tag{11}$$

which is the value of f_i on $\mathbf{P}$ for the next time step. Here $A_{\mathbf{P}}$ is the total area, $\text{Collision}_{\mathbf{P}}$ is the sum of Eq. (7), and $\text{Flux}_{\mathbf{P}}$ is the sum of Eq. (4), respectively. In other words, let $f_i(\mathbf{x},n\Delta t)$ be denoted by f_i^n, f_i^{n+1} is obtained. Eqs. (9) and (10) allow us to calculate $\mathbf{u}^{n+1}$. We add a correction step for velocity $\mathbf{u}^{n+1}$ to eliminate outward normal vector components of $\mathbf{u}^{n+1}$. The outward unit normal vector $\mathbf{n}^v$ can be calculated as

$$\mathbf{n}^v=\frac{\sum_{q\in I(\mathbf{P})}w_q\mathbf{n}_q}{|\sum_{q\in I(\mathbf{P})}w_q\mathbf{n}_q|}, \tag{12}$$

where $I(\mathbf{P})$ is the indexed set of one-ring neighboring points of $\mathbf{P}$, $\mathbf{n}_q$ is the outward directional unit normal vector of neighboring triangle T_q and w_q is the square inverse of distance between $\mathbf{P}$ and centroid $\mathbf{G}$, i.e., $w_q=1/|\overrightarrow{PG}|^2$. See [34,38,39] for further information about velocity correction. The velocity field is corrected by vector projection, Eq. (13). Fig. 3(c) shows the schematic illustration of velocity correction.

$$\mathbf{u}^{n+1}=\mathbf{u}^{n+1}-(\mathbf{u}^{n+1}\cdot\mathbf{n}^v)\mathbf{n}^v. \tag{13}$$

Finally, we update $f_i^{eq,n}$ to $f_i^{eq,n+1}$ using Eq. (8) with the updated density and corrected velocity field. Repeat this entire section for the next time step.

3. Numerical results

In this section, various experiments of fluid flows on curved 3D surfaces are demonstrated to illustrate the proposed method. Two layers of vortices are placed on a sphere to demonstrate Kelvin–Helmholtz instability (KHI) and storm behavior. Numerical experiments are conducted using various relaxation values, and the computational results are illustrated accordingly.

3.1. Kelvin–Helmholtz instability on discretized coastlines

Now, we consider the KHI which consists of two layers of vortices on a sphere with a radius of $R=10$. The marker function is defined as follows:

$$\phi_1(\mathbf{x})=\begin{cases}\tanh\left(\frac{R\theta-12.5\pi/3-\cos(10\psi)}{0.25\sqrt{2}}\right) & \text{if } z>0,\\ \tanh\left(\frac{-R\theta+17.5\pi/3+\cos(10\psi)}{0.25\sqrt{2}}\right) & \text{otherwise,}\end{cases} \tag{14}$$

where $\theta=\cos^{-1}(z/r)$, $\psi=\tanh^{-1}(y,x)$, and $r=\sqrt{x^2+y^2+z^2}$. For the two layers of vortices, the initial velocity field is defined as follows:

$$\mathbf{u}_1(\mathbf{x},0)=(0.01y\phi_1,\ -0.01x\phi_1,\ 0). \tag{15}$$

We use $\Delta t=0.01$ to conduct simulations until $t=10$. We use $\tau_{land}=1$ and $\tau_{sea}=1,\ 10$ to confirm the effect of the variable relaxation time value for the KHI on a sphere. Figs. 4(a) and (b) show snapshots of KHI on a sphere for $\tau_{land}=\tau_{sea}=1$ and $\tau_{land}=1$, $\tau_{sea}=10$, at time $t=0,\ 6,\ 10$ from left to right. The relation between the relaxation parameter τ and the kinematic viscosity ν in NS equation is given as $\nu=c_s^2(\tau-1/2)\delta_t$, where c_s is speed of sound. The kinematic viscosity is the ratio of dynamic viscosity to the density of the fluid defined as $\nu=\eta/\rho$, where η is dynamic viscosity and ρ is density. Fig. 4 shows temporal evolution of maximum velocity $\max\|\mathbf{u}\|$ for $\tau_{land}=\tau_{sea}=1$ and $\tau_{land}=1$, $\tau_{sea}=10$. From the result of Fig. 4(c), we can observe a gradual decrease in the velocity field overall after the occurrence of KHI within the same relaxation time $\tau_{land}=\tau_{sea}=1$. On the other hand, when $\tau_{land}=1$ and $\tau_{sea}=10$, localized turbulence occurs in areas with relatively high kinematic viscosity, such as the sea.

3.2. Storm behavior at $\tau_{land}=\tau_{sea}$

Storm behaviors and evolution in different phases are popular subjects of study. Wang et al. [40] provided a dynamic model consisting of a gaseous and particle phases to describe flow in a dust storm. Bousso et al. [41] also proposed a model for mixed flows in stormwater systems, using multiple phases such as air and water. Hession et al. [42] presented a two-phase Monte Carlo method to understand the evolution and propagation of hydrological and water quality models. Guardado-France et al. [43] studied storms from andesite sea cliffs on Isla San Luis Gonzaga, considering numerous phases depending on the geological location.

Using the same triangular mesh and coastline data, we added a storm to our globe model with a radius of 10. The center of the storm is located at $(-2.7063,-9.0583,3.2593)$ and the storm has a radius of 4. The two layers of vortices introduced in Section 3.1 are substituted for the numerical demonstration of storm behaviors. Fig. 5 illustrates the initial state of the globe model.

In this section, we test the storm model with the same relaxation time value τ on all points. i.e., $\tau=\tau_{land}=\tau_{sea}$ and we do not distinguish whether a point is on land or sea. We calculated the results for $\tau=1$ and 10 until the final time $T=10$. Fig. 6(a) and (b) shows the snapshots of the numerical solution on a sphere at times $t=0.5,\ 5$, and 10. Fig. 6(c) shows that the maximum of the $\|\mathbf{u}\|$. We observe that at $\tau=10$, compared to $\tau=1$, kinematic viscosity increases, leading to accelerated fluid flow, which causes velocities to cancel out and merge, resulting in relatively large oscillations. Additionally, when $\tau=1$, lower kinematic viscosity compared to $\tau=10$ causes velocities to monotonic decrease over time due to viscosity effects, particularly after a certain point in time.

3.3. Storm behavior at $\tau_{land}\neq\tau_{sea}$

In this section, we test the storm model with land and sea having different τ values. We fix $\tau_{land}=1$ and change τ_{sea} values to 1 and 10.

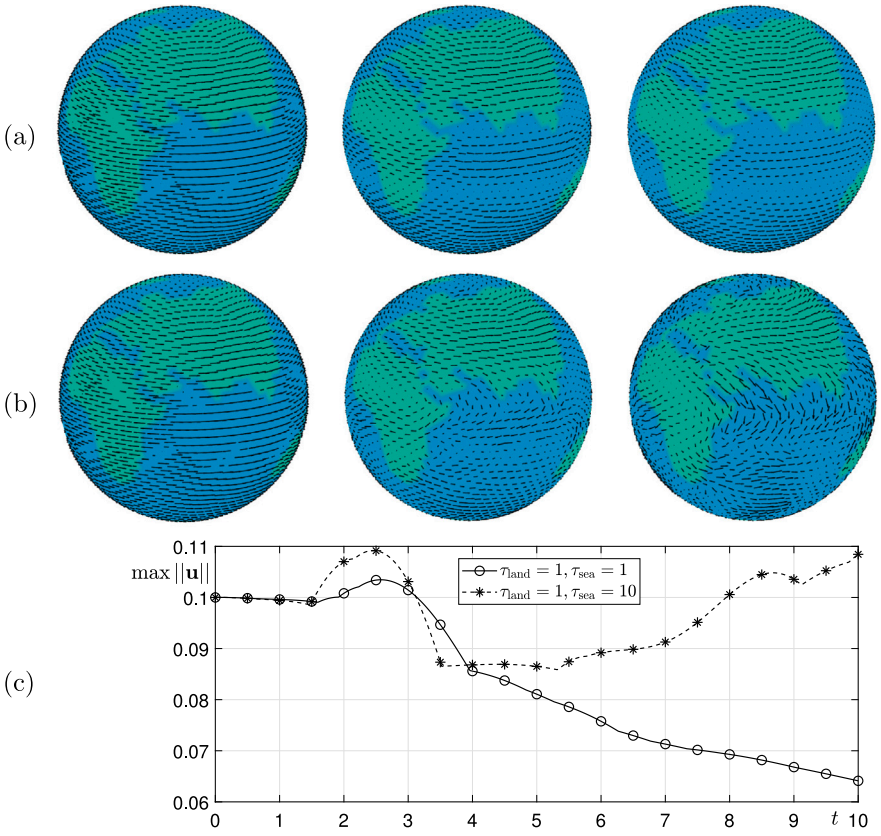

Fig. 4. Snapshots of KHI on a sphere for (a) $\tau_{land} = \tau_{sea} = 1$ and (b) $\tau_{land} = 1$, $\tau_{sea} = 10$, at time $t = 0,\ 6,\ 10$ from left to right. (c) $\max \|\mathbf{u}\|$.

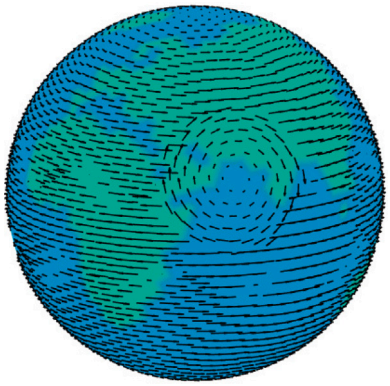

Fig. 5. Initial state after adding a storm.

Fig. 7(a) and (b) shows the snapshots of the numerical solution on a sphere at times $t = 0.5,\ 5$, and 10. Fig. 7(c) shows that the maximum of the $\|\mathbf{u}\|$. We can observe that the numerical simulation results are similar to those in Fig. 4. However, the width of the oscillations is larger due to the influence of the storm.

Finally, we consider a storm landing at the southwest of North America. The two layers of vortices are not included for this experiment. The initial state is shown in the left column of Fig. 8. The parameters are unchanged as in previous simulations. In the first simulation, we set $\tau_{land} = \tau_{sea} = 1$ and display the results in the top row of Fig. 8. The bottom row shows the results with respect to $\tau_{land} = 3.5$ and $\tau_{sea} = 1$. With the increase in τ_{land}, we observe that the velocity field dissipates faster on land.

4. Conclusions

In this paper, we presented an efficient numerical method for simulating incompressible fluid flow with variable viscosity on a spherical surface. We triangulated the spherical surface and simplified the coastlines using an interpolation. Therefore, it reduced calculation and achieved high efficiency. Then, the finite volume LBM was applied to solve incompressible fluid flows. The velocity field remains tangential to the surface through the velocity correction technique at each time step in the numerical method. Validation of the proposed method was conducted through various numerical tests, such as the evolution of a two-layer vortex and a storm. Computational results showed that our method is efficient for simulating incompressible fluid flow with

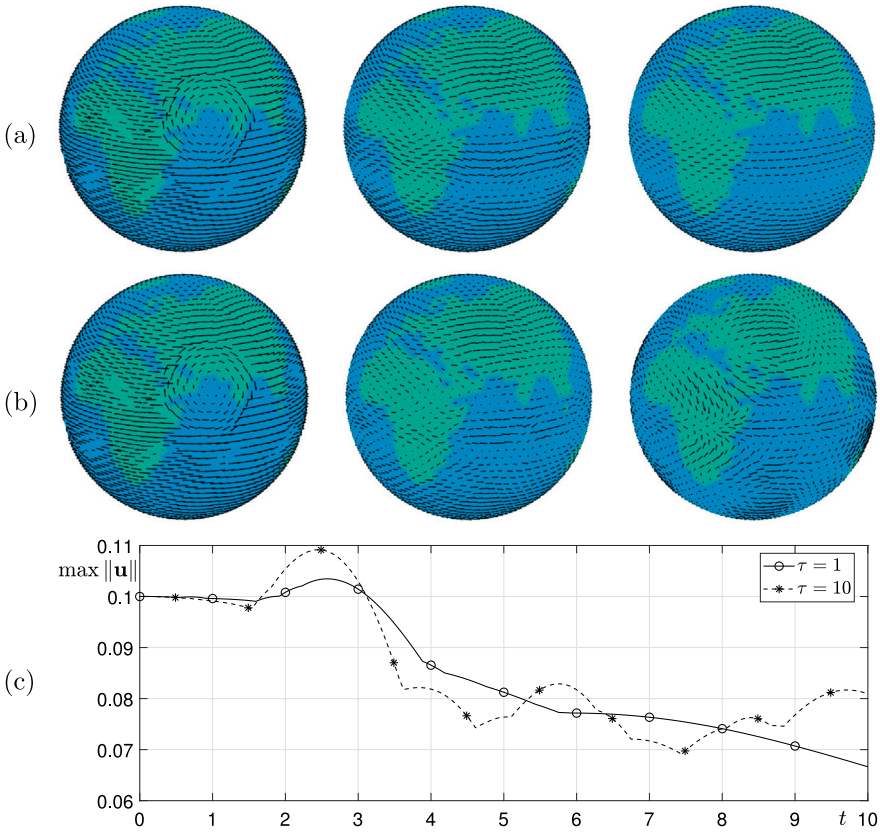

Fig. 6. Snapshots of the numerical solution on a sphere at times $t = 0.5,\ 5$, and 10 from left to right. (a) $\tau = 1$ and (b) $\tau = 10$ on both land and sea areas. (c) $\max \|\mathbf{u}\|$.

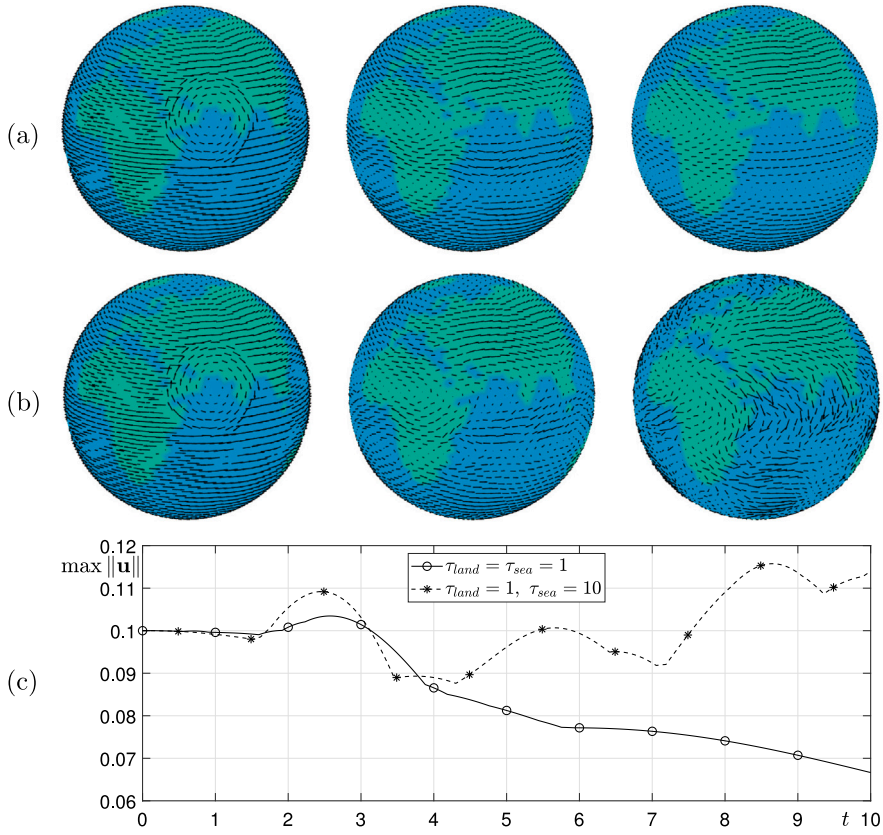

Fig. 7. Snapshots of the numerical solution on a sphere at times $t = 0.5,\ 5$, and 10 from left to right. (a) $\tau_{land} = \tau_{sea} = 1$ and (b) $\tau_{land} = 1,\ \tau_{sea} = 10$. (c) $\max \|\mathbf{u}\|$.

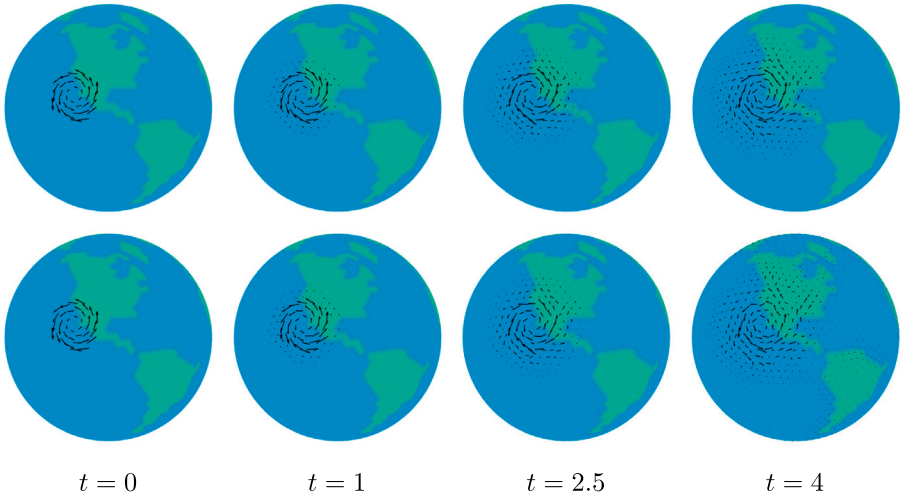

Fig. 8. Effect of τ_{land} on a storm landing at the southwest of North America. The top and bottom rows show the results with τ_{land} = 3.5 and 1, respectively. Here, τ_{sea} = 1 is fixed.

variable viscosity. For future work, we will extend the current method to include multiphase fluid flows [44–47] and data assimilation for weather modeling [48].

CRediT authorship contribution statement

Junxiang Yang: Writing – review & editing, Writing – original draft, Visualization, Validation, Software, Methodology, Investigation, Data curation. **Seungyoon Kang:** Writing – review & editing, Writing – original draft, Visualization, Software, Resources, Methodology, Investigation, Data curation. **Youngjin Hwang:** Writing – review & editing, Writing – original draft, Resources, Investigation, Data curation. **Soobin Kwak:** Writing – review & editing, Writing – original draft, Resources, Methodology, Data curation. **Seokjun Ham:** Writing – review & editing, Writing – original draft, Software, Resources, Investigation. **Junseok Kim:** Writing – review & editing, Writing – original draft, Visualization, Validation, Supervision, Software, Project administration, Methodology, Investigation, Funding acquisition, Formal analysis, Conceptualization.

Declaration of competing interest

The authors declare that they have no known competing financial interests or personal relationships that could have appeared to influence the work reported in this paper.

Data availability

No data was used for the research described in the article.

Acknowledgments

Junxiang Yang is supported by Macau University of Science and Technology Faculty Research Grants (FRG) (No. FRG-24-026-FIE). The corresponding author (J.S. Kim) was supported by the National Research Foundation of Korea(NRF) grant funded by the Korea government(MSIT) (No. 2022R1A2C1003844). The authors are thankful to the reviewers for their insightful feedback provided during the revision stage of this article.

References

[1] Chen S, Doolen GD. Lattice Boltzmann method for fluid flows. Annu Rev Fluid Mech 1998;30(1):329–64.
[2] Aidun CK, Clausen JR. Lattice-Boltzmann method for complex flows. Annu Rev Fluid Mech 2010;42:439–72.
[3] Wolf-Gladrow DA. Lattice-gas cellular automata and Lattice Boltzmann models: an introduction. Berlin: Soringer; 2000.
[4] Succi S. The Lattice Boltzmann equation for fluid dynamics and beyond. Oxford: Oxford University Press; 2001.
[5] Guo Z, Shu C. Lattice Boltzmann method and its applications in engineering. Singapore: World Scientific; 2013.
[6] Krüger T, Kusumaatmaja H, Kuzmin A, Shardt O, Silva G, Viggen EM. The Lattice Boltzmann method: principles and practice. Cham: Springer; 2017.
[7] Huang H, Sukop M, Lu X. Multiphase Lattice Boltzmann methods: Theory and applications. Chichester: Wiley; 2015.
[8] Wang H, Yuan X, Liang H, Chai Z, Shi B. A brief review of the phase-field-based Lattice Boltzmann method for multiphase flows. Capillarity 2019;2(3):33–52.
[9] Zhang Y, Dong B, An X, Wang Y, Zhou X, Li W. Phase-field-based Lattice Boltzmann model for ternary fluid flows considering the wettability effect. Appl Math Model 2022;103:195–220.
[10] Zheng L, Zheng S, Zhai Q. Reduction-consistent Cahn–Hilliard theory based Lattice Boltzmann equation method for N immiscible incompressible fluids. Phys A 2021;574:126015.
[11] Abdullah MM, Albargi HB, Malekshah EH, Sharifpur M. Thermal and hydrodynamic study of mixed convection heat transfer of a nanofluid in an enclosure with unequal-sized baffles using the Lattice Boltzmann method. Eng Anal Bound Elem 2023;153:201–12.
[12] Ebrahimi N, Ashtiani HAD, Toghraie D. Lattice Boltzmann method for mixed convection of nanofluid two-phase flow in a trapezoidal-shaped sinusoidal cavity by considering Brownian motion. Eng Anal Bound Elem 2023;152:194–213.
[13] Alqaed S, Mustafa J, Almehmadi FA, Alharthi MA, Elattar HF, Refaey HA, Aybar HŞ. Entropy generation of the laminar and mixed flow of alumina/water nanofluid flow in a two-dimensional rectangular enclosure affected by a magnetic field using the Lattice Boltzmann method. Eng Anal Bound Elem 2023;151:187–98.
[14] Ma C, Wu J, Gu X, Yang L. A three-dimensional high-order flux reconstruction Lattice Boltzmann flux solver for incompressible laminar and turbulent flows. Comput & Fluids 2023;265:106008.
[15] Mandzhieva R, Subhankulova R. Practical aspects of absolute permeability finding for the Lattice Boltzmann method and pore network modeling. Phys A 2021;582:126249.
[16] Babanezhad M, Nakhjiri AT, Marjani A, Shirazian S. Pattern recognition of the fluid flow in a 3D domain by combination of Lattice Boltzmann and ANFIS methods. Sci Rep 2020;10(1):1–13.
[17] Li QZ, Lu ZL, Chen Z, Shu C, Liu YY, Guo TQ. A simplified Lattice Boltzmann model for two-phase electro-hydrodynamics flows and its application to simulations of droplet deformation in electric field. Appl Math Model 2023;122:99–126.
[18] Hosseini SA, Atif M, Ansumali S, Karlin IV. Entropic Lattice Boltzmann methods: A review. Comput & Fluids 2023;105884.

[19] Barraza JAR, Deiterding R. Towards a generalised Lattice Boltzmann method for aerodynamic simulations. J. Comput. Sci. 2020;45:101182.
[20] Wittmann M, Haag V, Zeiser T, Köstler H, Wellein G. Lattice Boltzmann benchmark kernels as a testbed for performance analysis. Comput & Fluids 2018;172:582–92.
[21] Konig B, Fares E, Murayama M, Ito Y, Yokokawa Y, Yamamoto K, Ishikawa K. Lattice-Boltzmann simulations of the JAXA JSM high-lift configuration. In: 34th AIAA applied aerodynamics conference. 2016, p. 3721.
[22] He X, Luo LS, Dembo M. Some progress in Lattice Boltzmann method. Part I. Nonuniform mesh grids. J Comput Phys 1996;129(2):357–63.
[23] Nannelli F, Succi S. The Lattice Boltzmann equation on irregular Lattices. J Stat Phys 1992;68(3):401–7.
[24] Stiebler M, Tölke J, Krafczyk M. An upwind discretization scheme for the finite volume Lattice Boltzmann method. Comput & Fluids 2006;35(8–9):814–9.
[25] Wang Y, Zhong C, Cao J, Zhuo C, Liu S. A simplified finite volume Lattice Boltzmann method for simulations of fluid flows from laminar to turbulent regime, Part I: Numerical framework and its application to laminar flow simulation. Comput Math Appl 2020;79(5):1590–618.
[26] Wen M, Li W, Zhao Z. A hybrid scheme coupling Lattice Boltzmann method and finite-volume Lattice Boltzmann method for steady incompressible flows. Phys Fluids 2022;34(3).
[27] Hussain A, Afzal S, Rizwana R, Malik MY. MHD stagnation point flow of a Casson fluid with variable viscosity flowing past an extending/shrinking sheet with slip effects. Phys A 2020;553:124080.
[28] Chen Z, Shu C, Tan D. Immersed boundary-simplified Lattice Boltzmann method for incompressible viscous flows. Phys Fluids 2018;30(5).
[29] Guan Y, Novosselov I. Two relaxation time Lattice Boltzmann method coupled to fast Fourier transform Poisson solver: Application to electroconvective flow. J Comput Phys 2019;397:108830.
[30] He B, Lu S, Gao D, Chen W, Lin F. Lattice Boltzmann simulation of double diffusive natural convection in heterogeneously porous media of a fluid with temperature-dependent viscosity. Chinese J Phys 2020;63:186–200.
[31] Li S, Dimitrienko YI. Mathematical modeling for the local flow of a generalized Newtonian fluid in 3D porous media. Appl Math Model 2022;105:551–65.
[32] Chai Z, Shi B. Multiple-relaxation-time Lattice Boltzmann method for the Navier–Stokes and nonlinear convection–diffusion equations: Modeling, analysis, and elements. Phys Rev E 2020;102(2):023306.
[33] Zhao Y, Wu Y, Chai Z, Shi B. A block triple-relaxation-time Lattice Boltzmann model for nonlinear anisotropic convection–diffusion equations. Comput Math Appl 2020;79(9):2550–73.
[34] Yang J, Tan Z, Kim S, Lee C, Kwak S, Kim J. Finite volume scheme for the Lattice Boltzmann method on curved surfaces in 3D. Eng Comput 2022;38(6):5507–18.
[35] MATLAB and mapping toolbox release. Natick, Massachusetts, United States: The MathWorks, Inc.; 2022.
[36] Peng G, Xi H, Duncan C, Chou SH. Lattice Boltzmann method on irregular meshes. Phys Rev E 1998;58(4):R4124.
[37] Peng G, Xi H, Duncan C, Chou SH. Finite volume scheme for the Lattice Boltzmann method on unstructured meshes. Phys Rev E 1999;59(4):4675.
[38] Yang J, Li Y, Kim J. A practical finite difference scheme for the Navier–Stokes equation on curved surfaces in R3. J Comput Phys 2020;411:109403.
[39] Chen SG, Wu JY. Estimating normal vectors and curvatures by centroid weights. Comput Aided Geom Design 2004;21(5):447–58.
[40] Wang X, Wang T, Tang J, Gu F. Thermal diffusion characteristics of atmosphere-particle two phase flow in dust storm. Heat Mass Transf 2005;41:306–14.
[41] Bousso S, Daynou M, Fuamba M. Numerical modeling of mixed flows in storm water systems: critical review of literature. J Hydraul Eng 2013;139(4):385–96.
[42] Hession WC, Storm DE, Haan CT. Two-phase uncertainty analysis: An example using the universal soil loss equation. Trans ASAE 1996;39(4):1309–19.
[43] Guardado-France R, Johnson ME, Ledesma-Vázquez J, Santa Rosa-del Rio MA, Herrera-Gutiérrez ÁR. Multiphase storm deposits eroded from andesite sea cliffs on Isla San Luis Gonzaga (Northern Gulf of California, Mexico). J Mar Sci Eng 2020;8(7):525.
[44] Choi Y, Kim J. Maximum principle preserving and unconditionally stable scheme for a conservative Allen–Cahn equation. Eng Anal Bound Elem 2023;150:111–9.
[45] Yang J, Li Y, Kim J. A correct benchmark problem of a two-dimensional droplet deformation in simple shear flow. Mathematics 2022;10(21):4092.
[46] Xia Q, Kim J, Li Y. Modeling and simulation of multi-component immiscible flows based on a modified Cahn–Hilliard equation. Eur J Mech B-Fluids 2022;95:194–204.
[47] Xia Q, Sun G, Yu Q, Kim J, Li Y. Thermal-fluid topology optimization with unconditional energy stability and second-order accuracy via phase-field model. Commun Nonlinear Sci Numer Simul 2023;116:106782.
[48] Xia B, Yu R, Song X, Zhang X, Kim J. An efficient data assimilation algorithm using the Allen–Cahn equation. Eng Anal Bound Elem 2023;155:511–7.